Structure of 2-(2-(anthracen-9-ylmethylene)hydrazinyl)-4-(3-methyl-3-phenylcyclobutyl)thiazole by combined X-Ray crystallographic and molecular modelling studies

Tuncay Karakurt, Alaaddin Cukurovali & İbrahim Kani

Published online: 28 Jan 2020.

Submit your article to this journal

View related articles

View Crossmark data

Citing articles: 4 View citing articles

Taylor & Francis
Taylor & Francis Group

RESEARCH ARTICLE

Check for updates

Structure of 2-(2-(anthracen-9-ylmethylene)hydrazinyl)-4-(3-methyl-3-phenylcyclobutyl)thiazole by combined X-Ray crystallographic and molecular modelling studies

Tuncay Karakurt [a], Alaaddin Cukurovali [b] and İbrahim Kani [c]

aDepartment of Chemical and Process Engineering, Faculty of Engineering-Architecture, Kırsehir Ahi Evran University, Kirsehir, Turkey; bDepartment of Chemistry, Faculty of Science, Firat University, Elazig, Turkey; cDepartment of Chemistry, Faculty of Science, Eskisehir Technical University, Eskisehir, Turkey

ABSTRACT
A single crystal of 2-(2-(anthracen-9-ylmethylene)hydrazinyl)-4-(3-methyl-3-phenylcyclobutyl) thiazole ($C_{29}H_{25}N_3S$) containing anthracene, thiazole and cyclobutane rings has been synthesised. The synthesised crystal structure was characterised using IR, ^{1}H-NMR and ^{13}C-NMR spectroscopic and X-Ray analysis techniques. In the crystal, neighbouring molecules formed chains along [110] by interconnecting with N–H···N hydrogen bonding and $\pi-\pi$ interactions. The geometrical parameters of the title compound were optimised by Gaussian 09 software in the gas phase and Quantum-Espresso software under Periodic Boundary Conditions (PBC) in the solid phase. Theoretically, IR, NMR spectra, Mulliken, NPA and AIM atomic charges, Hirshfeld surface and frontier molecular orbitals (FMOs) of the title compound were examined. Using the Hirshfeld surface and two-dimensional (2D) fingerprint graphics, the presence of intermolecular interactions in the crystal packing were analysed. The energies of these interactions and their distribution on the crystal structure were shown graphically. In general, it was seen that theoretical calculations were consistent with X-Ray results.
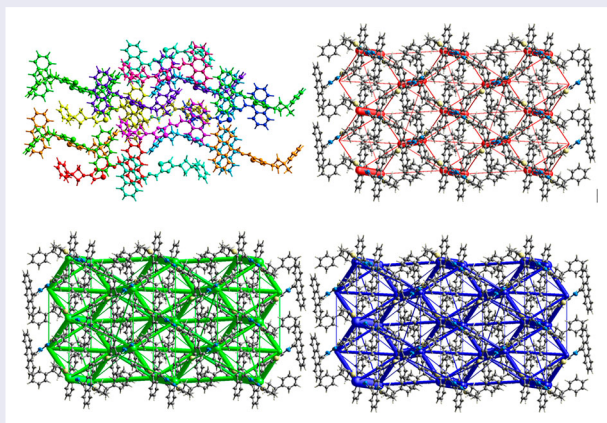
1. Introduction

Hydrazone-derived compounds, which are widely used in chemistry, have biological activity, light emission diodes (LEDs) [1–4] and chemosensory properties [5–10]. Dyes containing azo group have C=N or N=N groups. Azo dyes are widely used in the textile industry and because of their colour quality and ability to adhere to the fabric, azo dyes and derivatives are frequently used for dyeing different fabrics. The synthesis of azo dyes containing azo group and nitrobenzene group is well known in the literature [11]. Heterocyclic azo dyes have been reported to have positive effects against heat and light resistance, abrasion and fading after impregnation with different fabric types [12,13].

Compounds containing C=N group are called the Schiff bases. Since these compounds have properties such

as antibacterial, anticancer, antioxidant [14–16], antifungal, weed killer and insecticide [17], they are used as starting materials in the synthesis of many pharmaceutical substances. These compounds are used as a spectrophotometric reagent in analytical chemistry since they react to some metal ions [18]. Cu (II) complexes formed from Schiff base ligands have become essential model compounds in the study of the chemical and physical behaviour of biological copper systems [19]. Thiazole and its derivatives are important in biological systems as analgesics, antitumor and inhibitory and anti-inflammatory agents on lipoxygenase enzyme activities [20,21].

In this study, the structure of the synthesised new compound was confirmed using IR, ^{1}H-NMR, ^{13}C-NMR spectroscopic and X-Ray diffraction analysis techniques. Theoretically, the frontier molecular orbitals, Hirshfeld surface analysis, Mulliken, AIM and NPA atomic charges to investigate intermolecular interactions of the title compound, as well as NMR spectra in solution phase and IR spectra in gas phase were calculated.

2. Material and methods

2.1. X-Ray measurements and refinement

X-Ray diffraction data of the title crystals was collected with a Bruker APEX-II CCD [22] diffractometer using a MoKα radiation. Using Olex2 [23] program, the structure was solved by the SHELXT-2014 [24] software using direct methods. The SHELXL-2014 [25] software, which uses the full matrix least-squares method, was used to refine the location of the non-hydrogen atoms. Atomic coordinates of all hydrogen atoms were determined geometrically.

2.2. Synthesis and crystallization

To a solution of anthracene-9-carbaldehyde (2.0624 g, 10 mmol) in 50 mL of ethanol, a solution of thiosemicarbazide (0.9113 g, 10 mmol) in 20 mL of absolute ethanol was added in the presence of catalytic amount of p-toluene sulfonic acid and refluxed (TLC). After the mixture was cooled to room temperature, a solution of 2-Chloro-1-(3-methyl-3-phenylcyclobutyl)ethan-1-one (2.2271 g, 10 mmol) in 20 mL of absolute ethanol was

added dropwise. The mixture was kept at room temperature with continuous stirring for 2 h by checking the reaction course with IR. The solution was then made alkaline with an aqueous solution of NH$_3$ (5%), and light brown precipitate was separated by suction, washed with aqueous NH$_3$ solution several times and dried in air and crystallized from EtOH (Scheme 1). Yield: 58%, melting point: 455 K. Characteristic IR bands: 3127 cm^{-1} ν(–NH–), 2966–2874 cm^{-1} ν(aliphatics), 1618 cm^{-1} (C=N thiazole), 1568 cm^{-1} ν(C=N hydrazone), 733 cm^{-1} ν(C–S–C thiazole). Characteristic ^{1}H NMR shifts (CDCl$_3$, δ, ppm): 1.50 (s, 3H, –CH$_3$ on cyclobutane), 2.56–2.60 (m, 4H, –CH$_2$–, in cyclobutane ring), 3.75 (quintet, $j = 8.8$ Hz, 1H, >CH– in cyclobutane ring), 6.29 (s, 1H, =CH–S, in thiazole ring), 7.16–7.21 (s, 3H, aromatics), 7.31–7.35 (s, 2H, aromatics), 7.50–7.57 (m, 5H, aromatics), 8.03–8.04 (d, $j = 1.6$ Hz, 1H, aromatic), 8.05 (s, 1H, –NH–), 8.50 (s, 1H, azomethine), 8.67–8.69 (m, 2H, aromatics), 9.00 (s, 1H, aromatic). Characteristic ^{13}C NMR shifts (CDCl$_3$,
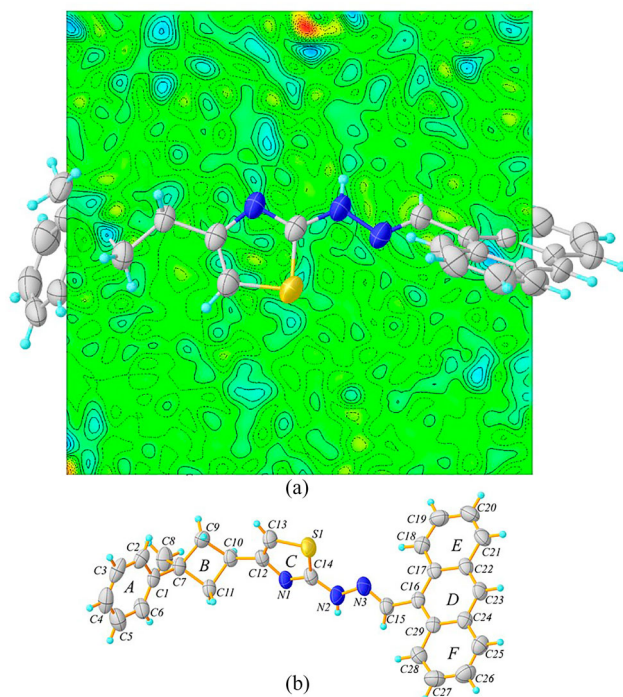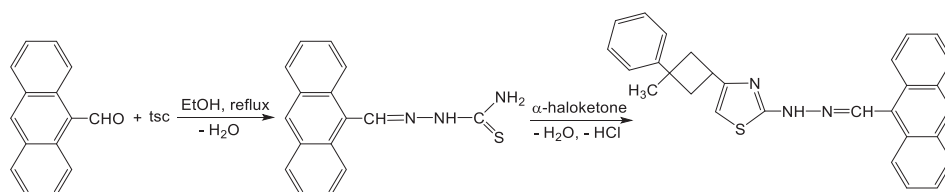

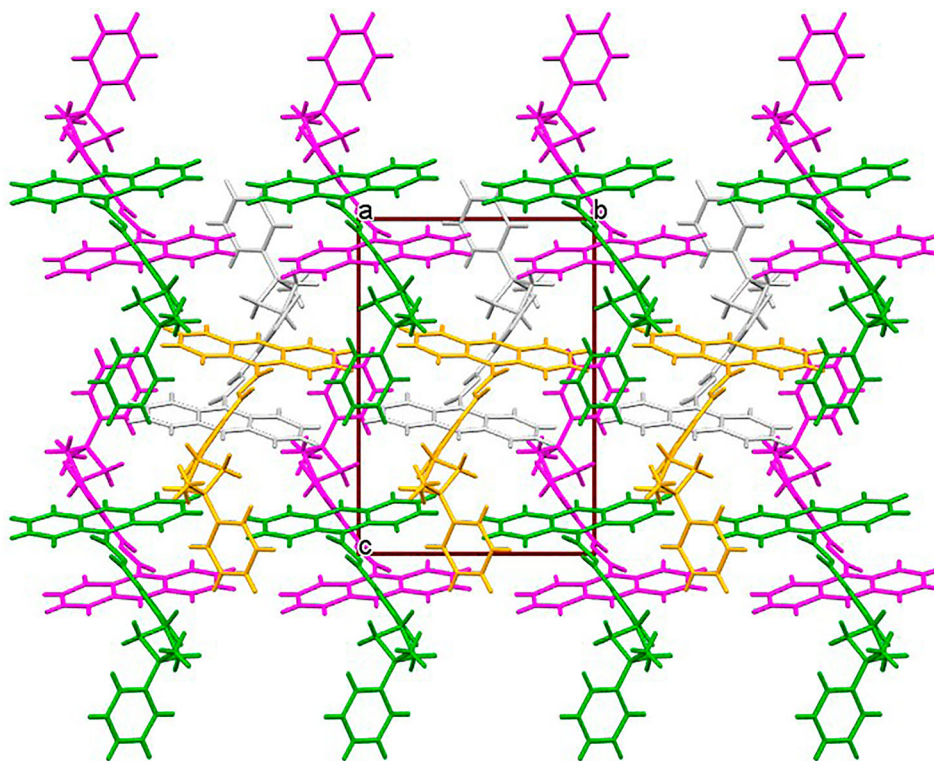**Figure 1.** (a) Difference fourier map (b) Experimental structure of the title crystal.

Scheme 1. Synthetic pathway for the synthesis of the target compound.

Table 1. Data collection and refinement values of $C_{29}H_{25}N_3S$ crystal.

Empirical formula	$C_{29}H_{25}N_3S$
Formula weight	447.58
Temperature/K	293(2)
Crystal system	monoclinic
Space group	$P2_1/c$
a/Å	13.645(4)
b/Å	11.026(4)
c/Å	15.953(5)
α/°	90
β/°	101.746(15)
γ/°	90
Volume/Å^3	2349.9(13)
Z	4
ρ_{calc}g/cm^3	1.265
μ/mm^{-1}	0.160
$F(000)$	944.0
Crystal size/mm^3	$0.22 \times 0.18 \times 0.08$
Radiation	MoKα ($\lambda = 0.71073$)
2Θ range for data collection/°	3.048 to 56.874
Index ranges	$-17 \leq h \leq 18, -14 \leq k \leq 14,$ $-17 \leq l \leq 21$
Reflections collected	35837
Independent reflections	5733 [$R_{int} = 0.0276, R_{sigma} = 0.0227$]
Data/restraints/parameters	5733/0/299
Goodness-of-fit on F^2	1.037
Final R indexes [$I \geq 2\sigma$ (I)]	$R_1 = 0.0539, wR_2 = 0.1394$
Final R indexes [all data]	$R_1 = 0.0855, wR_2 = 0.1614$
Largest diff. peak/hole/e Å^{-3}	0.51/−0.26
CCDC number	1953851

δ, ppm): 168.85, 155.86, 152.22, 140.08, 131.41, 130.11, 129.53, 129.04, 128.25, 126.92, 125.35, 124.95, 124.75, 101.99, 40.28, 38.89, 30.82, 30.07.

Table 2. The hydrogen bonding geometry of the title crystal (Å, °).

		D–H⋯A	D–H	H⋯A	D⋯A	D–H⋯A
X-Ray		C18–H18⋯N3	0.93	2.40	2.998(3)	122
		N2–H2N⋯N1^i	0.86	2.29	3.043(3)	147
Q-Espresso	LDA	C18–H18⋯N3	1.10	2.15	2.90	122
		N2–H2N⋯N1	1.08	1.68	2.76	172
	GGA	C18–H18⋯N3	1.09	2.27	2.97	121
		N2–H2N⋯N1	1.05	1.99	3.04	169

Notes: Symmetry code: (i) $1 - x, 1 - y, 1 - z$.

2.3. Computational details

The Gaussian 09 program [26], which uses the B3LYP [27,28] method and the 6–31G (d) [29] base set, was used for the theoretical calculations in gas phase of the title compound and GaussView 5 [30] program was used to visualise the results obtained from the theoretical calculations. Calculations in solid phase were made with Quantum Espresso 6.3 [31] program using periodic boundary conditions (PBC). These calculations were made using the density functional theory (DFT) [32] and the Perdew-Zunger (PZ) [33] pseudopotential (S/H/N/C.pz-van_ak.UPF) set under the Local Density Approach (LDA) and Perdew–Burke–Ernzerhof (PBE) [34] pseudopotential (S/H/N/C.pbe-van_bm.UPF) set under generalised gradient approximation (GGA). Finally, Hirshfeld surface [35] and Aim charge analysis calculations were performed using CrystalExplorer 17.5 [36] and AIMAII [37] programs, respectively.
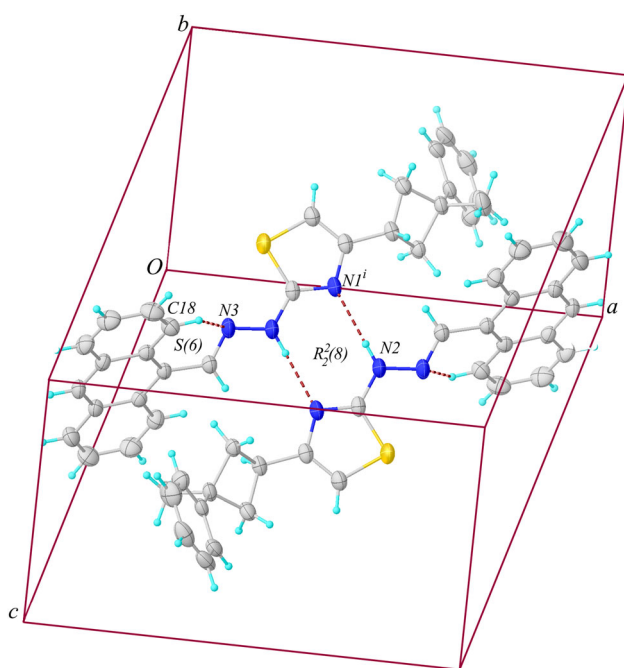

Figure 2. Representation of the title crystal ordered along *a* axis with symmetry operators.

Figure 3. Repetition of the title crystal by inter-intramolecular interactions.

3. Result and discussion

3.1. Geometrical structure of title compound

By looking at the fourier map (Figure 1a), it can be said that the H2N atom is positioned correctly since there is no proton deficiency or excess around the N1 and N2 atoms in the crystal. Details of the X-Ray data collection and structure refinement process of the title crystal are given in Table 1. The single crystal of $C_{29}H_{25}N_3S$ consist of A ($Cg1$) benzene, B ($Cg2$) cyclobutane, C ($Cg3$) thiazole and D ($Cg4$)/E ($Cg5$)/F ($Cg6$) anthracene rings (Figure 1b).

The maximum deviations from the planarity of the atoms of these rings were found to be 0.005 and −0.005

(C3 and C4 atoms), 0.131 (C10 atom), −0.002 (C12 atom) and −0.013 (C28 atom) Å. In addition, the planar angles between these rings are $A/B = 39.72$ (14)°, $B/C = 41.96$ (13)° and $C/D = 63.44$ (9)°. The cyclobutane ring is puckered by deviating from its planarity due to steric interaction between the side groups. This puckering angle in the cyclobutane ring was observed as being 26.88 (2)° and has been reported in the literature as being 25.98 (2)° [38]. Figure 2 shows the crystals ordered along the a-axis with symmetry operators. While the grey molecules repeat themselves with x, y, z symmetry operator, the pink molecules repeat with glide plane (Glide plane perpendicular to [0, 1, 0] with glide component [0, 0, 1/25]), the yellow molecules repeat the centre of inversion (inversion at [0, 0, 0]) and the green molecules repeat with the screw axis (2-fold) (2-fold screw axis with direction [0, 1, 0] at 0, y, 1/4 with screw component [0, 1/2, 0]) symmetry element.

When X-Ray diffraction results of the title crystal were examined, it was observed that, as expected, the double bond of C14=N1 in the thiazole ring is shorter than the single bond length of N1–C12. These bond lengths were found to be 1.303 (2) Å and 1.392 (3) Å, respectively. The double bond character C13=C12 bond length in the ring is 1.338 (3) Å, and the lengths of S1–C13 and S1–C14 were found to be 1.734 (2) Å and 1.728 (2) Å, respectively. These bond lengths are consistent with the values given in the literature for the thiazole ring [39]. In the crystal, dimer structure was formed by the intermolecular N–H⋯N hydrogen bonds which characterised by an $R_2^2(8)$ motif and the intramolecular C–H⋯N interactions, which characterised by an S (6) motif, stabilise the conformation of the monomer structure. N2 atom (symmetry code: x, y, z) has formed the N2–H2N⋯N1 hydrogen bonding with N1 (symmetry code: $1−x, 1−y, 1−z$), by acting like a donor atom. There are also three weak $\pi-\pi$ interactions in the molecular ordering within the title crystal. These interactions took
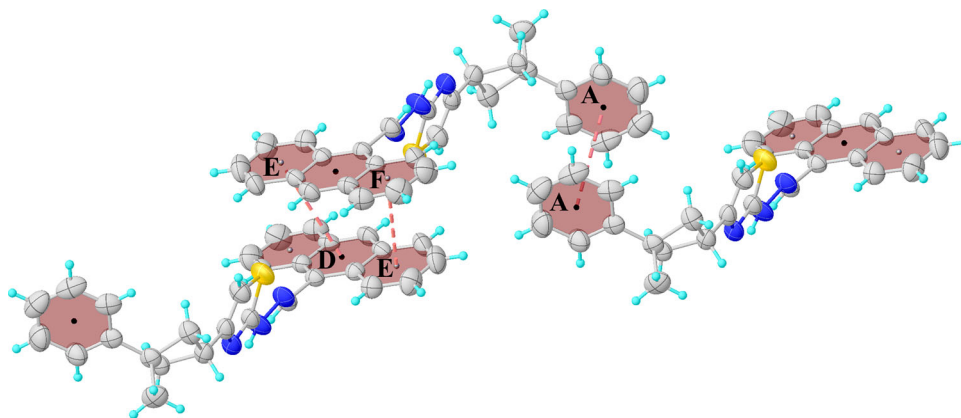

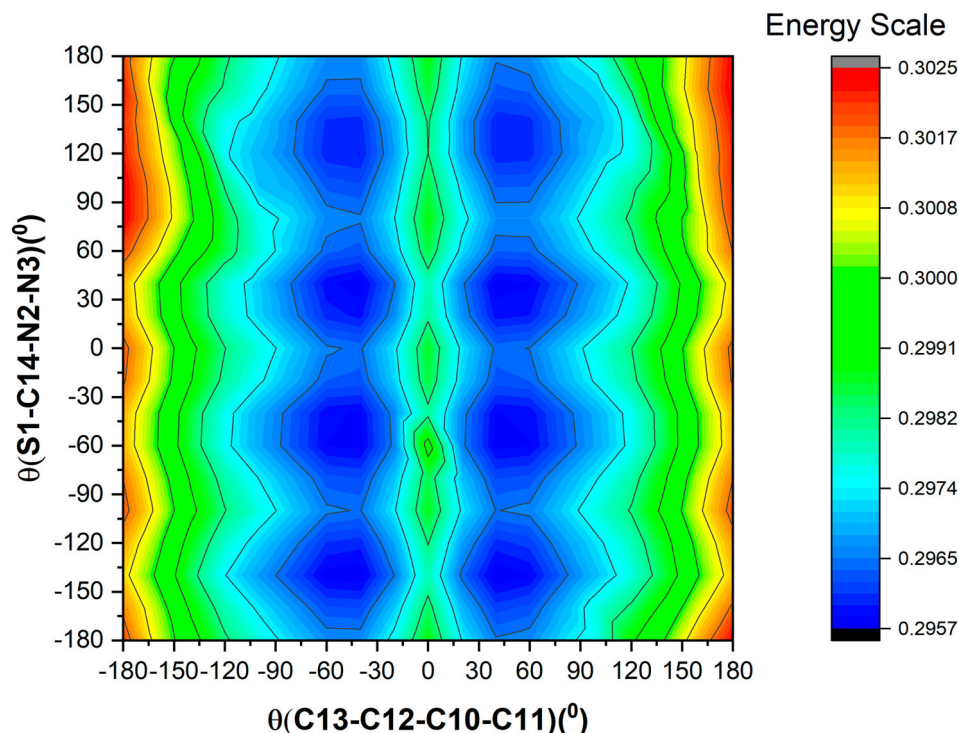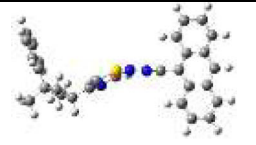**Figure 4.** Packing of the title crystal with $\pi-\pi$ interactions along the a axis.
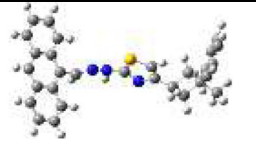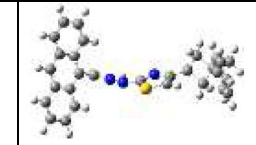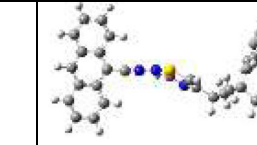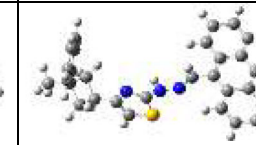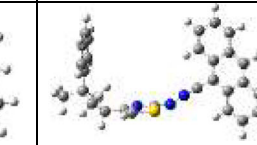
Figure 5. 3D PES analysis graph of the title molecule.

Table 3. Conformation of the title molecule.

-1682.515798 a.u.	-1682.515495 a.u.	-1682.515509 a.u.	-1682.516061 a.u.
μ= 1.018148 *D*	μ= 0.786667 *D*	μ= 0.808983 *D*	μ= 1.023647 *D*
Conf1	Conf2	Conf3	Conf4
-1682.515845 a.u.	-1682.518423 a.u.	-1682.518427 a.u.	-1682.515577 a.u.
μ= 0.861879 *D*	μ= 0.816899 *D*	μ= 0.843845 *D*	μ= 0.845708 *D*
Conf5	Conf6	Conf7	Conf8

place between the *A* (*Cg1*)–*A* (*Cg1*), *E* (*Cg5*)–*D* (*Cg4*) and *E* (*Cg5*)–*F* (*Cg6*) rings. As a result of these interactions, the ring systems are arranged in parallel with each other and the nearest perpendicular distance is 3.922 (2) Å between the centres of the *A* rings and 3.8176 (18) Å between the centres of the *E* and *D* rings, and also 3.8038 (19) Å between the centres of the *E* and *F* rings. Symmetry information of hydrogen bonding interactions are given in Table 2. The N–H··· N, C–H···N and
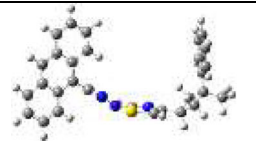
π–π interactions in the unit cell are shown in Figures 3 and 4.

Theoretically, 3-dimensional potential energy surface scan (PES) was performed using the AM1 (Austin Model 1) [40] semiempirical method for the $\theta 1$(C13–C12 –C10–C11) and $\theta 2$(S1–C14–N2–N3) dihedral angles to determine local minimum points of the title compound. Dihedral angles were changed in the range from −180 to 180° for 10° steps and single-point energies were

Figure 6. Calculated optimise structure of the title compound.

Table 5. Comparison of the experimental and optimised unit-cell parameters calculated by the Quantum ESPRESSO (QE) VC-Relax method of the title crystal.
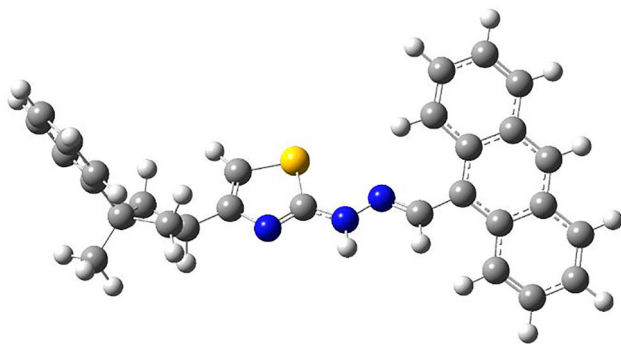
Experimental	QE-VC-Relax	QE-VC-Relax
Space group P21/c	Space group P21/c LDA	Space group P21/c GGA
$a = 13.645(4)$ Å	$a = 13.185$ Å	$a = 13.84950$ Å
$b = 11.026(4)$ Å	$b = 10.659$ Å	$b = 11.19874$ Å
$c = 15.953(5)$ Å	$c = 15.393$ Å	$c = 16.04186$ Å
$\beta = 101.75(15)°$	$\beta = 105.24°$	$\beta = 101.39007°$
$Z = 4$	$Z = 4$	$Z = 4$
$V = 2350(13)$ Å³	$V = 2087$ Å³	$V = 2439$ Å³

calculated in each step. As a result of the PES analysis (Figure 5), 8 conformations (Table 3) corresponding to local minimum points were obtained. All the conformational structures were optimised by DFT/B3LYP/6–31G (d) method and these optimised structures are shown in Table 3. As shown in Table 3, Conf7 structure is the most stable structure with the smallest energy relative to other conformations (Figure 6). The Conf7 structure was used to calculate geometric parameters of the optimised molecule using Gaussian 09 software.

The X-Ray diffraction data, calculated bond lengths, bond angles and torsion angles in the gas and solid phase of the $C_{29}H_{25}N_3S$ crystal are given in Table 4.

LDA with PZ pseudopotential and GGA with PBE pseudopotential approaches were used for the solid phase calculations. The root mean square error (RMSE) values, which are determined in order to understand the agreement between the parameters calculated in gas and solid phase and experimental data, are presented in Table 4. When the RMSE values are examined, it is seen that GGA approach is more successful in representing experimental geometry than other methods for all geometric parameters.

3.2. Periodic boundary calculations (PBC)

The coordinates of 232 atoms in the unit cell were obtained from the cif file of the title crystal and the each energy value was calculated by changing kinetic energy

Table 4. Experimental and calculated geometric parameters of the title compound in gas and solid phases.

Bond lengths (Å)	X-Ray Diffraction	Gas Phase	Solid Phase (LDA)	Solid Phase (GGA)
S1–C13	1.734(2)	1.752	1.721	1.734
S1–C14	1.728(2)	1.758	1.732	1.749
N2–N3	1.379(2)	1.348	1.348	1.378
N3–C15	1.275(3)	1.290	1.293	1.302
N1–C14	1.303(2)	1.301	1.317	1.320
N1–C12	1.392(3)	1.388	1.378	1.397
N2–C14	1.364(3)	1.372	1.344	1.357
C12–C13	1.338(3)	1.363	1.362	1.371
C7–C9	1.550(3)	1.565	1.544	1.563
C10–C11	1.548(3)	1.559	1.538	1.554
C1–C6	1.382(3)	1.401	1.393	1.406
C1–C2	1.381(3)	1.401	1.389	1.402
C1–C7	1.505(3)	1.517	1.490	1.512
C16–C17	1.422(3)	1.426	1.417	1.428
RMS		0.01466	0.015818	0.011894
Bond Angles (°)				
C12–N1–C14	109.89(17)	110.34	110.85	110.18
C14–N2–N3	117.28(17)	121.28	117.32	117.46
C13–S1–C14	87.90(10)	87.32	88.42	88.25
C9–C7–C11	87.38(14)	87.88	88.15	87.81
N2–N3–C15	114.88(17)	117.44	114.95	114.40
C5–C6–C1	121.40(2)	121.01	120.96	121.19
RMS		1.802044	0.43175	0.286914
Dihedral Angles (°)				
N1–C12–C10–C11	62.10(2)	68.56	61.20	62.12
N3–N2–C14–S1	−12.20(3)	−2.10	−8.37	−11.85
N1–C12–C13–S1	−0.30(2)	0.17	−0.45	−0.90
N2–N3–C15–C16	173.58(18)	−178.21	169.24	171.77
N1–C12–C10–C9	167.54(17)	174.95	168.08	168.65
RMS		148.438867	2.554348	1.253062

Table 6. Experimental and theoretical ^{1}H and ^{13}C isotropic chemical shift values of the title molecule (with respect to TMS, all values in ppm).

Atoms	Experimental in solution	DFT in solution
C1	152.22	145.1
C2	124.95	117.22
C3	130.11	120.25
C4	129.04	117.48
C5	130.11	120.22
C6	124.95	117.32
C7	38.89	40.33
C8	30.07	29.6
C9	40.28	36.85
C10	30.82	31.57
C11	40.28	40.99
C12	155.86	147.87
C13	101.99	102.28
C14	168.85	165.2
C15	152.22	132.05
C16	131.41	120.16
C17	131.41	122.67
C18	129.53	120.09
C19	128.25	120.89
C20	126.92	118.74
C21	129.53	122.63
C22	140.08	123.9
C23	124.75	124.79
C24	140.08	123.15
C25	129.53	123.55
C26	125.35	118.4
C27	125.35	120.33
C28	129.53	117.03
C29	131.41	124.31
–NH–	8.05	11.25
Azomethine	8.67–8.69	9.16
=CH–S	6.29	5.73
–CH$_2$–cyclobutane ring	2.56–2.60	2.05–2.47
Benzene ring	7.16–7.35	6.59–7.03
CH3	1.5	0.12–0.52
Anthracene ring	7.50–9.0	7.56–9.18

cut-off (E_{cut}) between 10 and 200 Ry to determine the optimal E_{cut} for the system modelled in the plane wave self-compliance field program. In these calculations, LDA with Perdew-Zunger (PZ) pseudopotential and GGA with Perdew–Burke–Ernzerhof pseudopotential approaches were used. As can be seen from the figures (Figure 7a,b), it is seen that the total energy of the system converges towards a certain energy value as the E_{cut} value increases in both LDA and GGA approaches. Since the change in total energy after $E_{cut} \simeq 30$ Ry is very small, the effect on the system is also minimal. It is observed that there is no significant change in the total energy of the system after this value (~ 30 Ry). In addition, in order to define a lattice constant suitable for the system, by changing the lattice constant in the range from 13.1 to 14.2 a.u., total energy has been calculated for each value (Figure 7a,b). In this calculation, it was determined that the lattice constant value corresponding to the minimum energy of the system is a $\simeq 13.65$ a.u in both LDA and GGA approaches. For the calculations, k-point mesh was determined by MP (Monkhorst-Pack) method [41] and taken as $1 \times 1 \times 1$ in the Brillouin-zone.

In order to increase the accuracy of the results, a convergence value of 10^{-7} Rydberg (Ry) for energy calculation was used. Stable parameters of the unit cell were obtained by using the QE-VC-Relax option method and a Broyden-Fletcher-Goldfarb-Shanno (BFGS) quasi-Newton optimisation algorithm using the lattice constant ($a = 13.65$ a.u.) and energy cutoff ($E_{cut} = 30$ Ry). Table 5 shows the unit cell parameters obtained (X-Ray) and calculated (QE-VC-Relax), and Figure 8a–c shows the packing of atoms in the unit cell obtained from QE-VC-Relax and X-Ray.

3.3. IR studies

The dimer structure was optimised with DFT/B3LYP/6–31G(d) theory using X-Ray experimental atomic position of the title molecule (Figure 9). The vibration frequencies were calculated using the optimised dimer structure. The title compound has C1 point group symmetry with 58 atoms in symmetric unit and 171 fundamental vibration frequency. A scale factor of 0.9613 [42] was used to correct the calculated vibrational frequencies. Experimental and calculated spectra (obtained from dimer structure) are shown in Figure 10.

While the stretching vibration frequency of N–H group, which has made an intermolecular bonding, decreases, the bending vibration frequency increase [43]. While the free vibration frequency of N–H group peaks at 3500–3300 cm^{-1}, the bonded N–H group frequency occur in 3200–2400 cm^{-1} [44,45]. In our study, the vibration frequency of this mode was observed at 3127 cm^{-1} and calculated at 3119 cm^{-1}. In the literature, this frequency was reported at 3179 cm^{-1} and calculated at 3101 and 3075 cm^{-1} [46]. In-plane bending vibration frequency of NH group has been observed at 1494 and 1434–1586 cm^{-1} [46] in literature. This vibration mode was calculated at 1446–1583 cm^{-1}. The out-of-plane bending vibration frequency of this group was observed at 760 cm^{-1} and calculated at 716 cm^{-1}. Considering all these results, it can be concluded that the NH group has been used for intermolecular bonding. The vibrational frequencies of C=N (thiazole) and C=N (Hydrazone) of the other groups of the molecule were observed at 1618 and 1568 cm^{-1}, respectively, and are consistent with the literature [46]. These peaks were calculated at 1601 and 1565 cm^{-1}. In most hydrocarbons, CH$_2$ symmetrical stretching vibrations were expected to appear at 2900–2850 cm^{-1} ranges, while their asymmetric stretching vibrations were observed at 3000–2900 cm^{-1} [47]. In the present study, symmetrical and asymmetric CH$_2$ stretching vibrations were recorded at 2864 and 2966 cm^{-1}, respectively and calculated at 2950–2957 and 3004–3011 cm^{-1}.
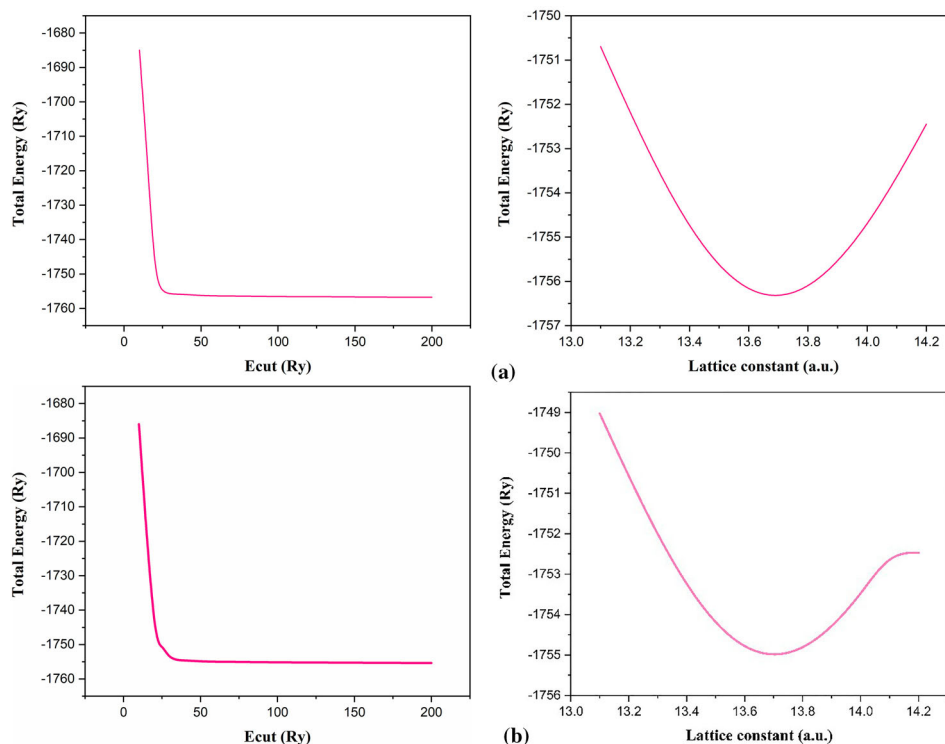
Figure 7. Total energy graphs according to Ecut and lattice constant (a) LDA, (b) GGA approaches.
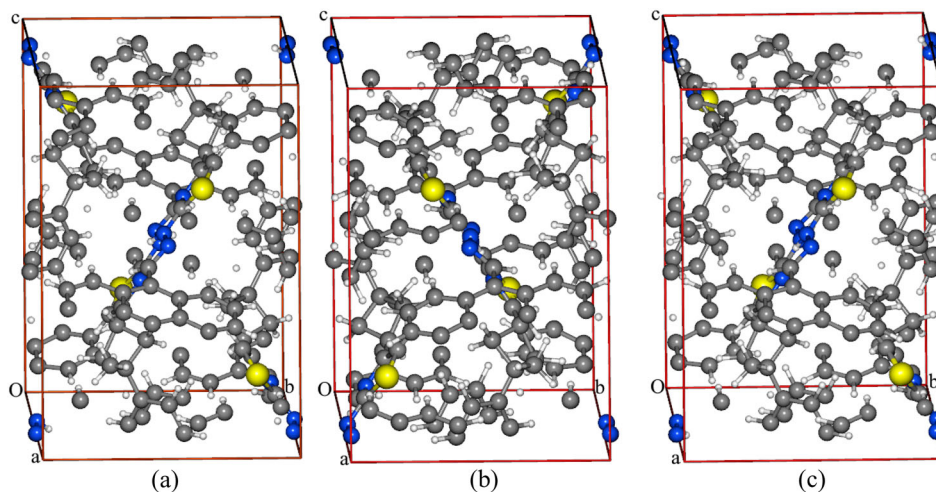

Figure 8. Representation of atoms within the unit cell of the title crystal (a) X-Ray, (b) LDA-*QE-VC-Relax*, (c) GGA-*QE-VC-Relax*.

3.4. NMR studies

The ^{13}C and ^{1}H NMR spectra were recorded on a Varian-Gemini 400 MHz spectrometer using tetramethylsilane (TMS) as the internal reference. GIAO (Gauge-Independent Atomic Orbital) [48,49] method and Gaussian 09 program were used to calculate chemical shift values of the isolated single molecule in solution (in CDCl$_3$ solution) and TMS molecule was taken as reference. Experimentally, when the ^{13}C-NMR spectrum of the compound is examined in Figure 11a, the peaks of C12 at 155.86 ppm, C13 at 101.99 ppm and C14

at 168.85 ppm indicate that the thiazole ring is formed. In particular, the C14 signal is larger than other carbon atoms due to the electronegative atoms (N and S atoms) around it. The chemical shift values of C12, C13 and C14 atoms were calculated at 147.87, 102.28 and 165.2 ppm, respectively.

Experimentally, in the ^{1}H-NMR spectrum (Figure 11b), the hydrogen peak of the NH group was experimentally observed at 8.05 ppm. As it is known, acidic proton peaks such as OH and NH were expected to appear at 1–14 ppm ranges. In the theoretical calculation, the value
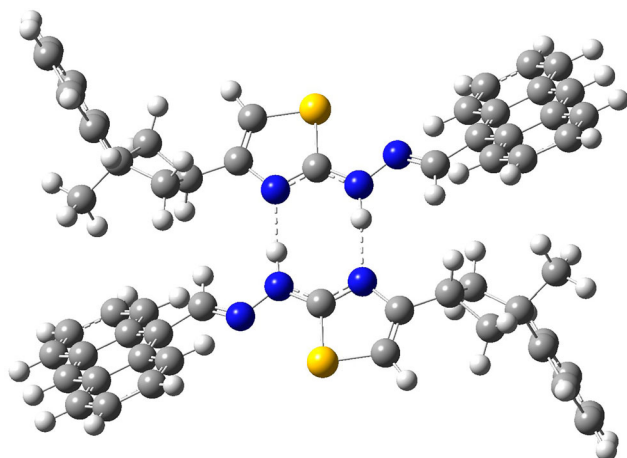
Figure 9. Representation of dimer structure of the title crystal.

Figure 10. Experimental and Theoretical IR spectra of the title compound.

of this peak was calculated at 11.25 ppm. The peak of azomethine group (−CH=N) was observed experimentally at 8.67–8.69 ppm and calculated at 9.16 ppm. The proton signal of the CH group in the thiazole ring was determined at 6.29 ppm and calculated at 5.73 ppm. The CH_3 and CH_2 proton peaks on the cyclobutane ring were observed at 1.5 and 2.56–2.60 ppm, respectively. These peaks were calculated at 0.12–0.52 and 2.05–2.47 ppm. Other NMR values of the synthesised compound are given in Table 6.

3.5. Frontier molecular orbitals (FMOs)

HOMO and LUMO orbital energy values were investigated on the optimised structure of the title compound. These orbitals describe intramolecular interactions. HOMO energy determines the tendency to give
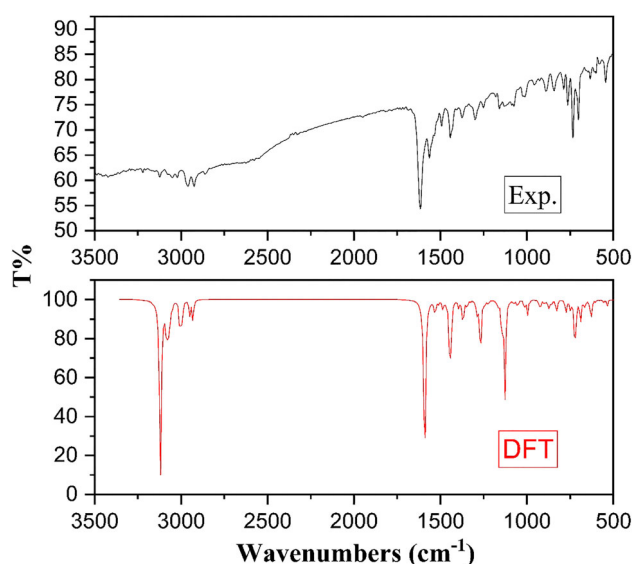
electrons and LUMO energy determines the tendency to take electrons. The small energy value between HOMO and LUMO explains the charge transfer interactions that occur within the molecule and are effective in chemical and biological activities [50] and initiates also charge transfer that makes the material active as NLO [51]. The molecular mechanism of the interaction area between the ligand-receptor at the quantum chemical level explains that it interacts with HOMO orbitals on the nucleophilic molecule (drug) and LUMO orbitals on the electrophilic receptor active site [52]. More favourable interactions between the high-value HOMO energy ligand and its receptor have been reported in previous studies [53].
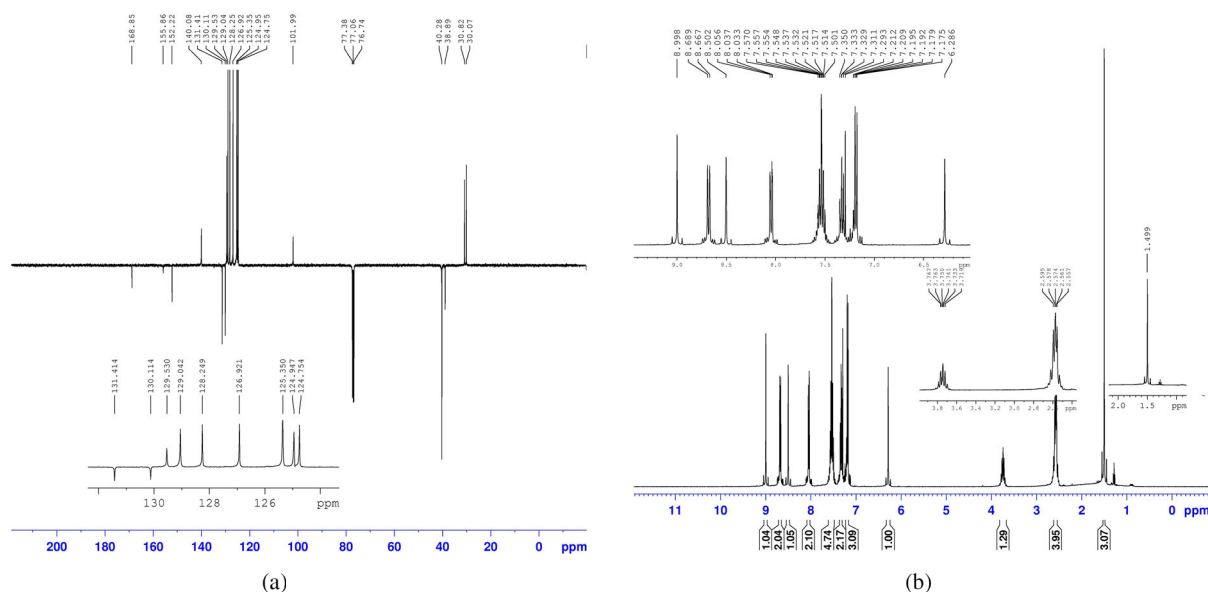

Figure 11. Experimental (a) ^{13}C NMR (b) ^{1}H NMR spectra of target compound in solution.

First Excited State —————— $E_{LUMO} = -2.04$ eV

$\Delta E = 2.99$ eV

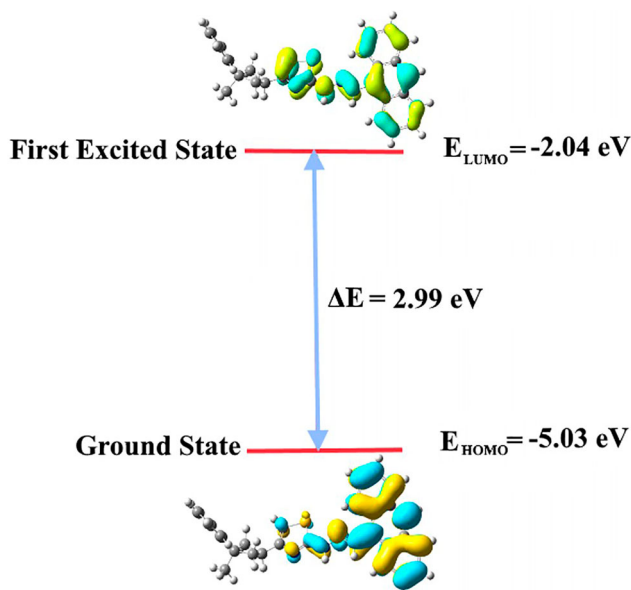**Ground State** —————— $E_{HOMO} = -5.03$ eV

Figure 12. Molecular orbital surfaces and energy levels for the HOMO and LUMO.

The calculations were carried out in the gas and solid phase, and the HOMO-LUMO energy values and the difference between these two orbitals were calculated as being −5.03, −2.04 and 2.99 eV in the gas, respectively and −3.05, −1.23 and 1.82 eV in the solid phase. As shown in Figure 12, the title molecule contains 118 occupied and 431 unoccupied molecular orbitals, the positive phase which is blue and the negative phase which is

yellow and the highest energy occupied HOMO is mainly localised on the N2 and N3 atoms and anthracen and thiazole rings, and the lowest energy unoccupied LUMO is mainly located on the N2 and N3 atoms and anthracen ring.

3.6. Mulliken, NPA, AIM charges and MEP analysis

For further information on the nature and strength of inter-intramolecular hydrogen bonding interactions within the title molecule, the QTAIM approach of the Bader, Mulliken and NPA charge analyses were used.

To give information about the strength and characteristics of a chemical bond, electron density (ρ_{BCP}), Laplacian of electron density ($\nabla^2(\rho_{BCP})$), the potential energy density ($V(r)$) and the kinetic energy density ($G(r)$) at different bond critical points (BCPs) were calculated using the QTAIM approach. The total electron energy density ($H(r)$) was obtained by using formula $H(r) = G(r) + V(r)$ [54,55]. While $\nabla^2(\rho_{BCP})$ is negative in covalent bonds ($\nabla^2(\rho_{BCP}) < 0$), it is positive in bonds formed by ionic, Van der Waals and hydrogen interaction ($\nabla^2(\rho_{BCP}) > 0$). It has been reported as covalent hydrogen bonds; $\nabla^2(\rho_{BCP}) < 0$ and $H_{BCP} < 0$, medium hydrogen bonds in partial-covalent character; $\nabla^2(\rho_{BCP}) > 0$ and $H_{BCP} < 0$ and weak hydrogen bonds in electrostatic character; $\nabla^2(\rho_{BCP}) > 0$ and $H_{BCP} > 0$, according to Rozas et al. [56] based on the QTAIM
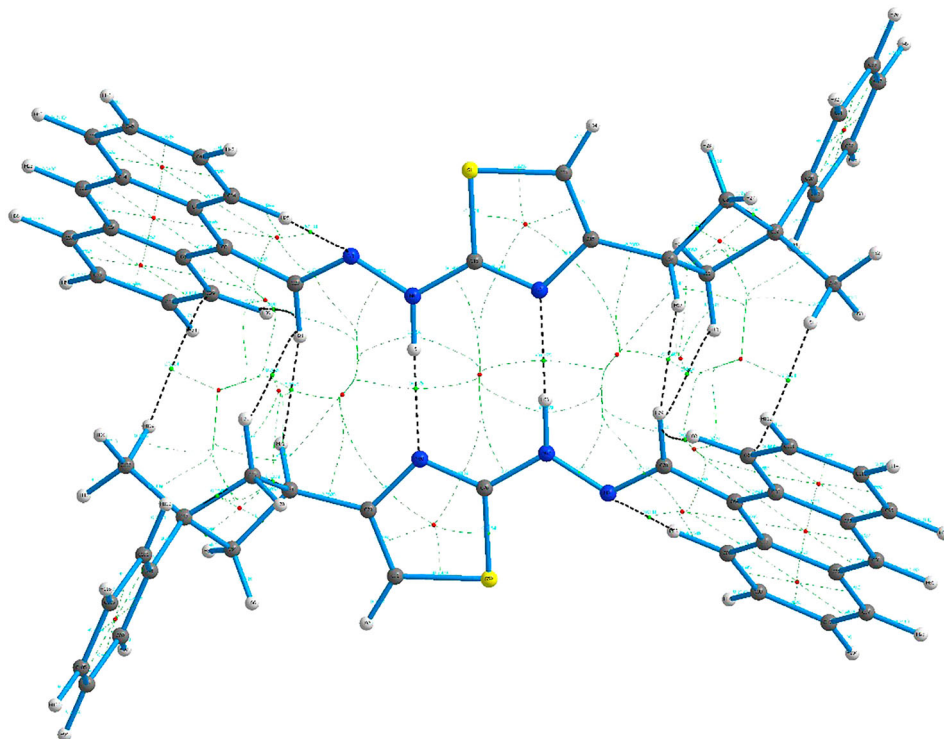

Figure 13. Molecular graph of dimer structure: bond critical points (small green spheres), ring critical points (small red sphere).

theory. According to the QTAIM theory, the interaction of the dimer structure using AIMAII program is shown in Figure 13.

Topological parameters of inter-intramolecular interactions are given in Table 7. As shown in Table 7, H_{BCP} value is negative for N2–H2N···N1 interaction and positive for C18–H18···N3 interaction. According to the criteria given by Rozas et al. and the literature [57], the intermolecular N2–H2N···N1 interaction is stronger than the intramolecular C18-H18···N3 interaction. Positive ρ_{BCP} and $\nabla^2 \rho_{BCP}$ values of both interactions showed that these interactions were natural electrostatic bindings. Also, the AIM approach could also be used to evaluate inter-intramolecular hydrogen bonding interactions. The presence of a bond critical point (BCP) and the bond path connecting two atoms together provide conclusive evidence of hydrogen bonding [58]. The relationship between interaction energy (E_{int}) and potential energy density was reported by Espinoza; $E_{int} = 1/2$ (V_{BCP}) [59]. These calculated E_{int} values are given in Table 7 and based on the E_{int} values, it can be said that the intermolecular N2–H2N···N1 interaction (E_{int} of −5.49 kcal/mol) is stronger than the intramolecular C18–H18···N3 interaction (E_{int} of −3.48 kcal/mol). Furthermore, as shown in Figure 13, there is weak C–H···π interaction between the C8 atom and the $Cg6$ ring with an interaction energy of −0.44 kcal/mol.

The Mulliken, NPA and AIM atomic charges which have been calculated from the optimised molecular geometry of the title crystal are given in Figure 14.

According to the results of the whole charge analyses, all hydrogen atoms in the molecule have positive charges.

The most negative atomic charges in the molecule is on the N1 (−0.57), N2 (−0.244) and N3 (−0.508) for Mulliken, N1 (−0.581), N2 (−0.264) and N3 (−0.387) for NPA and N1 (−1.228), N2 (−0.775) and N3 (−0.841) for the AIM analysis as well as the most positive atomic charge is on the H2N (0.396 for Mulliken, 0.390 for NPA, 0.483 for AIM) atom. The three methods displayed similar results to each other. According to all of these results, it can be said that N1, N2, N3 and H2N atoms could be used for inter-intramolecular interaction.

When the molecular potential map (MEP) (Figure 15a) of optimised geometry is examined, it is seen that the regions encoded with the most negative region that is determined by the red colour and the most positive region, which is determined by the blue colour, give equivalent results with partial charge values obtained from Mulliken, NPA and AIM analysis. Furthermore, the most negative atoms are clearly seen in orange regions in the secondary MEP map obtained from electron density (Figure 15b). In MEP plots (Figure 15a,b), the most negative regions were found to be on N1 (−0.039 a.u.) and N3 (−0.035 a.u.) atoms, and are consistent with the AIM, NPA and Mulliken charge analysis. In the same way, in Figure 15a, the most positive region is on the H2N (+0.048 a.u.) atom and it shows excellent with the results of AIM, NPA and Mulliken charge analysis. According to this results, N1 and N3 atoms are the most suitable

Table 7. Topological parameters for bonds of interacting atoms: electron density (ρ_{BCP}), Laplacian of electron density ($\nabla^2 \rho_{BCP}$), kinetic electron energy density (G_{BCP}), potential electron energy density (V_{BCP}), total electron energy density (H_{BCP}), hydrogen bond energy (E_{int}) at bond critical point (BCP).

Interaction	ρ_{BCP} (a.u.)	$\nabla^2 \rho_{BCP}$ (a.u.)	G_{BCP} (a.u.)	V_{BCP} (a.u.)	H_{BCP} (a.u.)	E_{int} (kcal/mol)
N2–H2N···N1	+0.0248	+0.0632	+0.0167	−0.0175	**−0.0008**	**−5.49**
C18–H18···N3	+0.0166	+0.0585	+0.0129	−0.0111	**+0.0018**	**−3.48**
C8–H8b···π	+0.0036	+0.0105	+0.0020	−0.0014	**−0.0006**	**−0.44**

Table 8. Interaction Energies (kJ/mol) between a reference molecule and its neighbours. R: the distance between molecular centroids (mean atomic position) in Å.

C	N	S	R	Interaction	$E_{electrostatic}$	$E_{polarization}$	$E_{dispersion}$	$E_{exchange-repulsion}$	E_{total}
	1	−x, −y, −z	15.65		−4.0	−0.4	−13.5	11.8	−9.0
	2	x, −y+1/2, z+1/2	18.21		−0.4	−0.2	−7.1	1.6	−5.8
	1	−x, −y, −z	10.49	*Cg4···Cg5/Cg5···Cg6*	−9.5	−3.5	−79.9	45.7	−54.0
	2	−x, y+1/2, −z + 1/2	17.09		−2.5	−0.4	−14.5	7.3	−11.1
	2	x, −y + 1/2, z + 1/2	17.84		−0.9	−0.2	−8.6	5.4	−5.2
	2	x, y, z	11.03		−1.4	−0.3	−9.9	7.6	−5.7
	2	−x, y + 1/2, −z + 1/2	8.81		−7.4	−3.0	−54.8	24.1	−42.9
	1	−x, −y, −z	13.95	*Cg1···Cg1*	−4.5	−1.5	−48.0	32.0	−27.8
	2	x, −y + 1/2, z + 1/2	9.36		−5.8	−0.9	−29.7	16.4	−22.5
	1	−x, −y, −z	5.28	**N2–H2N···N1**	−67.6	−15.3	−92.5	103.5	−99.4
	0	−x, −y, −z	11.67		0.1	−0.0	−1.7	0.0	−1.3

Notes: *C*: colour of each molecule; *N*: the number of equivalent neighbours; *S*: symmetry operator.
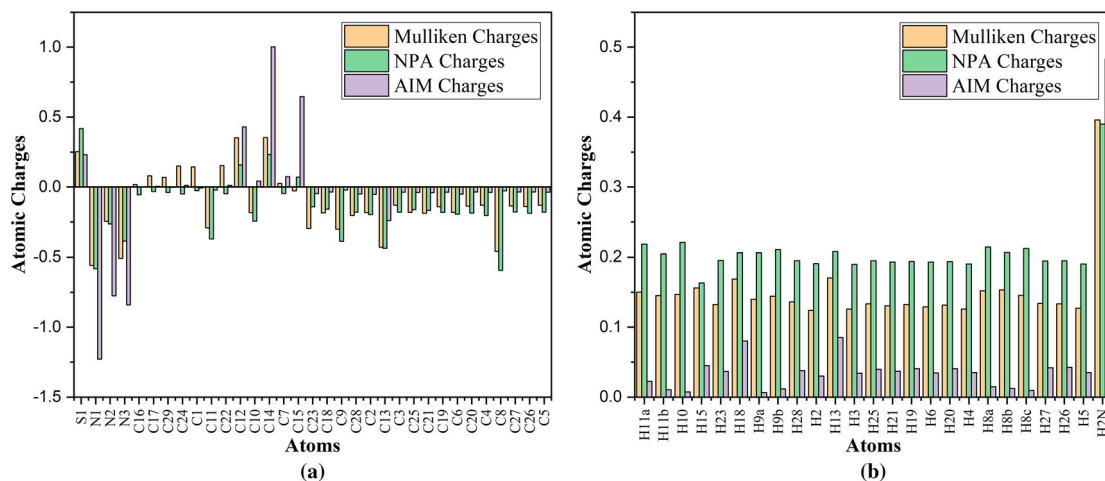
Figure 14. Mulliken, NPA and AIM charges of (a) non-hydrogen (b) hydrogen atoms of the title compound.
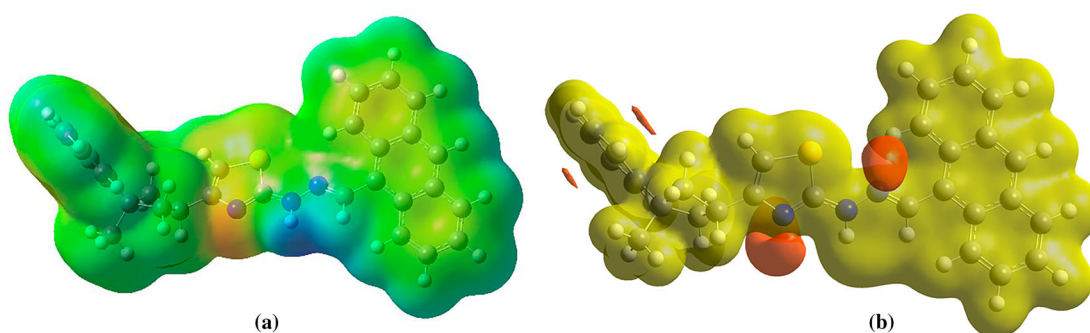

Figure 15. (a) Primary (b) secondary MEP surfaces obtained from the electron density of the title compound.

regions for electrophilic reaction and H2N atom is also the most suitable for nucleophilic reaction.

3.7. Hirshfeld surfaces

Hirshfeld surface analysis examining intermolecular interactions is also of great interest in the field of crystallography because it provides detailed information about

the solid-state behaviour of compounds, and the Hirshfeld surface (d_{norm}) is expressed by the following equation;

$$d_{norm} = \frac{d_i - r_i^{vdw}}{r_i^{vdw}} + \frac{d_e - r_e^{vdw}}{r_e^{vdw}}$$

In the equation, d_i is the distance from the Hirshfeld surface to the nearest nucleus inside and d_e
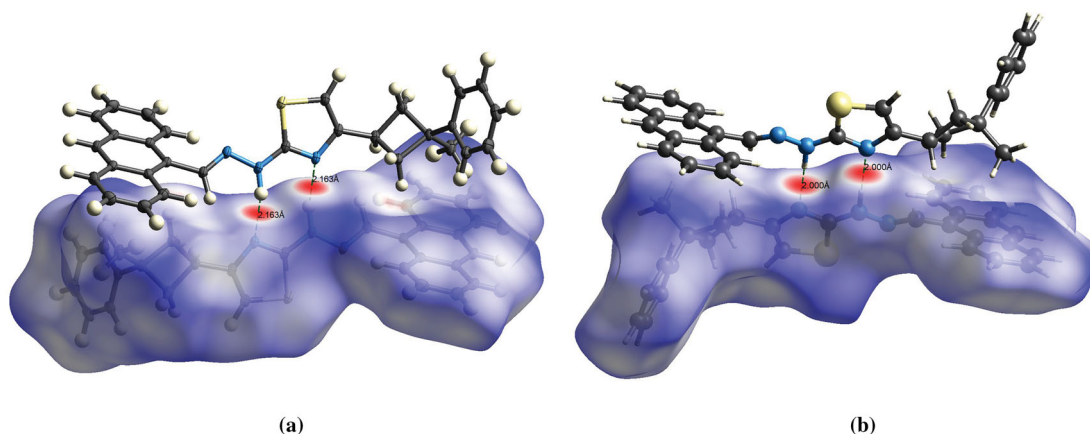

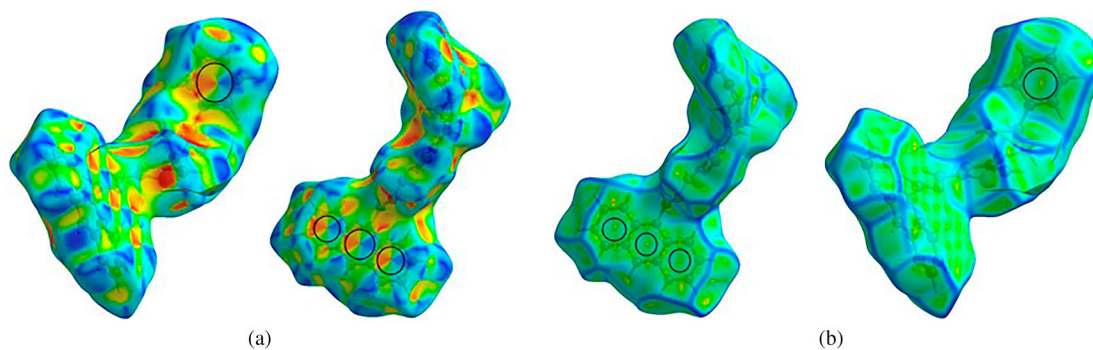**Figure 16.** d_{norm} Hirshfeld surfaces of structures obtained by (a) X-Ray (b) GGA-*QE-VC-Relax*.

Figure 17. The Hirshfeld surface mapped over (a) shape-index (b) over curvedness of title compound.

outside the surface. r_i^{vdw} and r_e^{vdw} represent van der Waals radii of atoms [60]. The red, blue and white regions in the Hirshfeld surface map associated with the d_{norm} indicate that the interatomic distance is smaller, greater and equal than the van der Waals radii sum, respectively [61]. The molecular electrostatic potentials
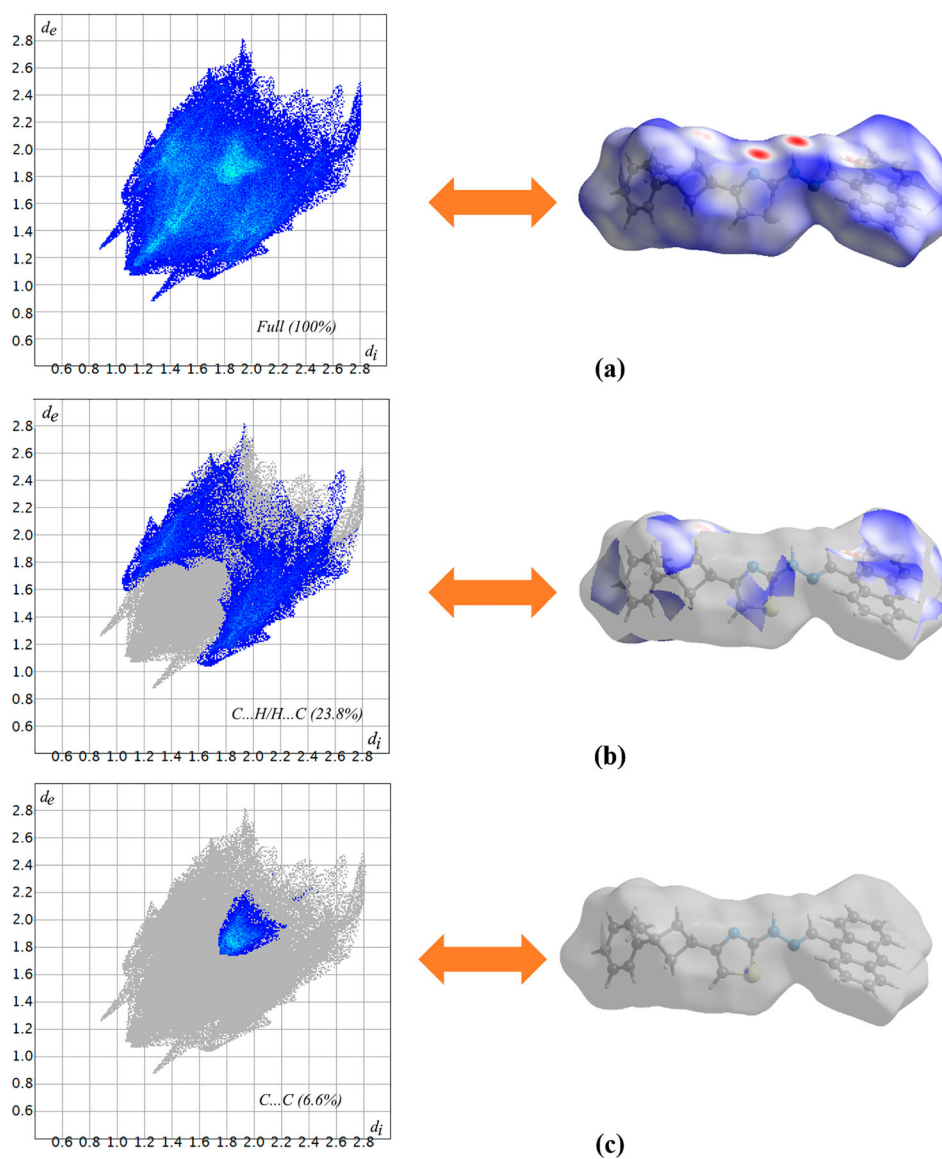

Figure 18. 2D fingerprint plots for the title compound, showing (a) all interactions (b) C⋯H/H⋯C % 23.8, (c) C⋯C % 6.6 (d) H⋯H % 53.7, (e) N⋯H/H⋯N % 8.1.
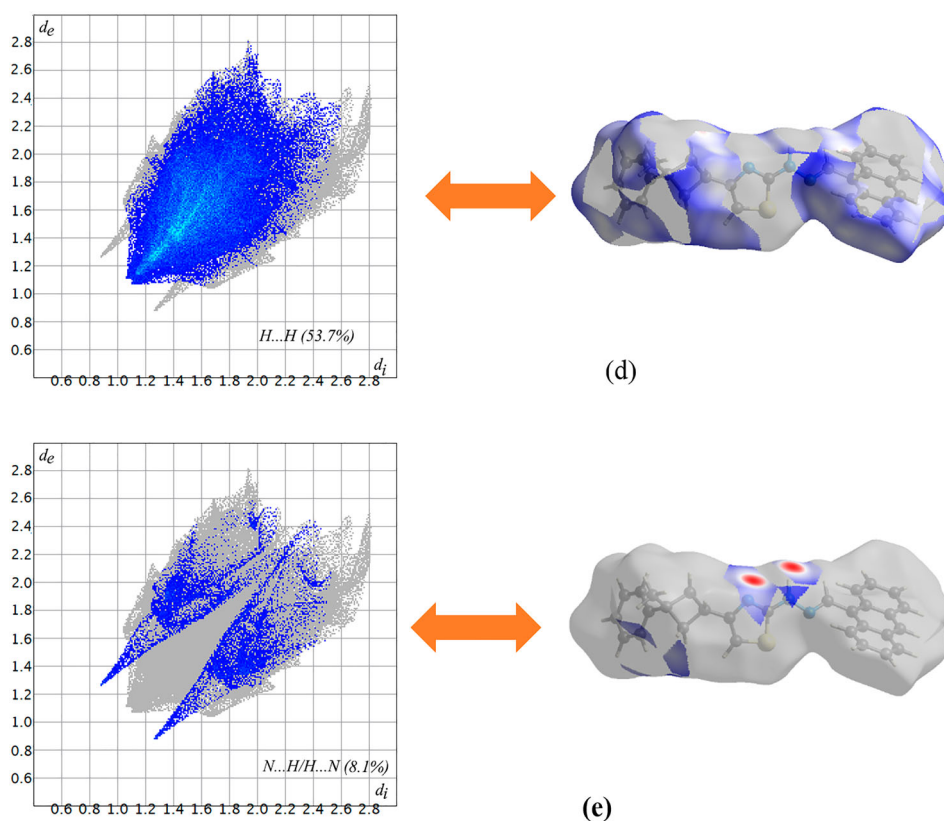
(d)

(e)

Figure 18. Continued.

of the three-dimensional Hirshfeld surfaces (d_{norm}) of the experimental and optimised structures obtained by the GGA method were −0.362 to +1.510 and −0.472 to +1.555 a.k.b. mapped on the colour scale using Hartee–Fock theory with STO-3G [62,63] basis set (Figure 16a,b). On Hirshfeld surfaces map obtained from the X-Ray structure, the two bright dark red spot circles that emerge on the d_{norm} surface represent strong N–H $\cdots$ N interactions which H2N $\cdots$ N1 interaction length is 2.163 Å (Figure 16a). Furthermore, the H2N $\cdots$ N1 interaction length in the structure obtained from GGA approach has been observed at 2.000 Å (Figure 16b) and shorter than the other.

The Hirshfeld shape index and curvedness surface describes π–π interactions that occur planarly between molecular pairs [64]. These interactions have been represented by red and blue adjacent 'triangles' in the shape index of the Hirshfeld surface. The Hirshfeld shape index is shown in Figure 17a, and the adjacent red and blue triangular symbols on the circled rings *Cg1* and *Cg4-6* indicate that these rings interact π–π between the molecular pairs. At the same time, these interactions on the curvedness surface are seen as flat regions on the ring (Figure 17b).

The 2D fingerprint represents a way to define and summarise the contact type of all interactions between

molecular pairs [65]. The 2D fingerprint graphs given in Figure 18 show the presence of H$\cdots$H, O$\cdots$H, N$\cdots$H and C$\cdots$H interactions in the crystal. H$\cdots$H interaction corresponds to 53.7% of the total interaction on the Hirshfeld surface, while C$\cdots$H/H$\cdots$C interactions to 23.8%, C$\cdots$C interactions to 6.6% and N$\cdots$H/H$\cdots$N interactions provide the lowest contribution with 8.1%.

The H$\cdots$N/N$\cdots$H contacts, which correspond to the N2–H2$\cdots$N1 hydrogen bonding, appear as two sharp symmetric spikes in the two-dimensional fingerprint map with a protruding long spike at $de + di = 2.13$ Å. The H$\cdots$H/H$\cdots$H contacts, which represent the short interatomic interactions, were represented by a single broad peak at $de = di \simeq 1.06$ Å in the middle of the scattered points on the two-dimensional fingerprint maps. The C$\cdots$C/C$\cdots$C contacts, which are the measure of π–π stacking interactions, are shown by a unique triangle at $de = di \simeq 1.75$ Å. The total interaction energy between molecular pairs is sum of the energies of the four major components including electrostatic, polarisation, dispersion, and exchange-repulsion components with scale factors of 1.057 (k_ele), 0.740 (k_pol), 0.871 (k_disp) and 0.618 (k_rep), respectively for benchmarked energy models [66]. These energies of the title compound were obtained using a dispersion-corrected CE-B3LYP/6-31G (d, p) quantum level of theory. The
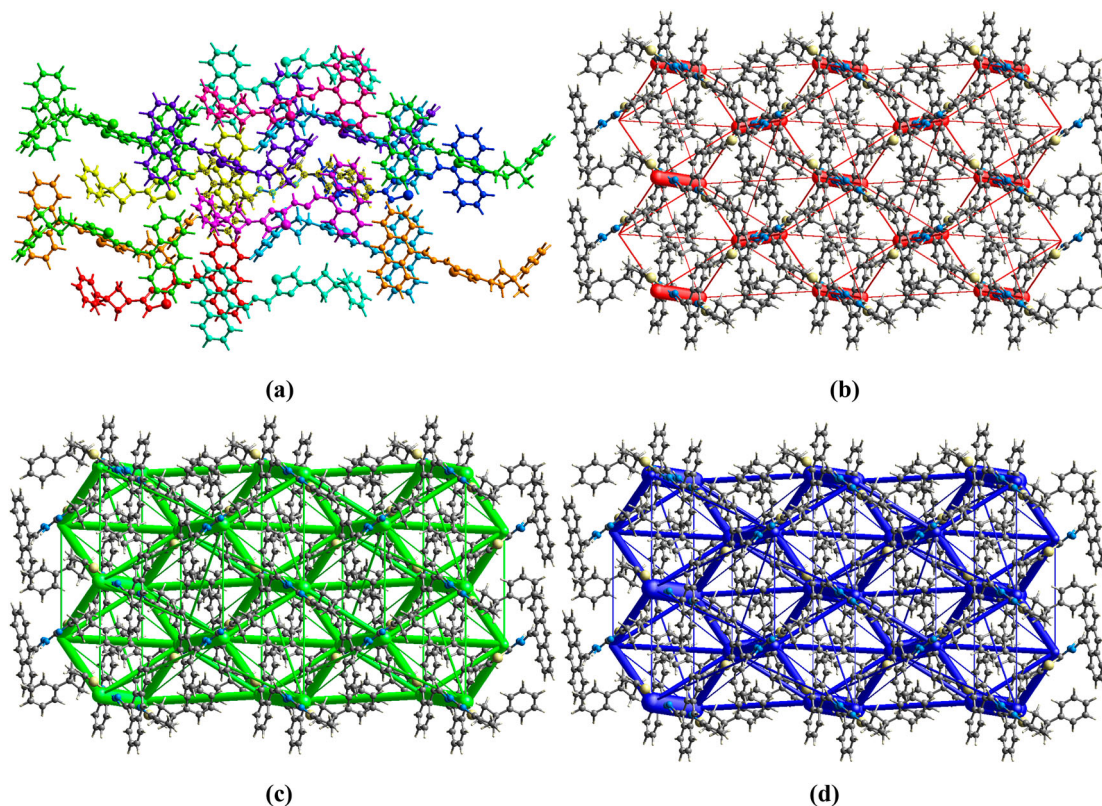
Figure 19. (a) Interactions between the reference molecule, which are indicated by yellow colour, and the molecules present within a radius of 3.8 Å (b) coulomb energy (red cylinders) framework, (c) dispersion energy (green cylinders) framework and (d) total energy (blue cylinders) framework.

energies were calculated using the Crystal-Explorer for the 3.8 Å radius cluster of molecules around a selected reference molecule. The data reported in Table 8 shows that crystal packaging in the title compound is mostly equilibrated with electrostatic, dispersion and exchange-repulsion components, and that the major contribution to electrostatic energy is due to the strong hydrogen bonding. In Figure 19a, within the supramolecular architecture, the magnitude of the four intermolecular interaction energies of the crystal structure is visualised in $2 \times 2 \times 2$ block unit cells using energy frames. The energy frameworks have been represented as cylinders that connect centroids of molecule pairs. The radius of these cylinders is proportional to the magnitude of the energy frameworks and is represented by red cylinders for E_{elec}, green for E_{dis} and blue for E_{tot} (Figure 19b–d). All energy frameworks were adjusted to the scale for tube/cylinder size of 100 with a cut-off value of 4 kJ/mol.

4. Conclusions

In this study, the structure of 2-(2-(anthracen-9-ylmethylene)hydrazinyl)-4-(3-methyl-3-phenylcyclobutyl)thiazole compound was elucidated by experimental and theoretical studies using X-Ray diffraction, IR and NMR

spectroscopic methods. In particular, the geometric parameters of the title compound were also calculated in the Solid phase. Nucleophilic and electrophilic reaction sites on the title molecule were determined by Mulliken, NPA and AIM charge analyses. The hydrogen bonding and $\pi-\pi$ interactions in the molecule were examined by calculating Hirshfeld surfaces of the title crystal. All interactions between the molecular pairs were elucidated in detail with 2D fingerprint graphics on the Hirshfeld surface. Finally, the interaction energies between the molecular pairs of the title compound were calculated using the Hirshfeld surface.

Disclosure statement

No potential conflict of interest was reported by the authors.

ORCID

Tuncay Karakurt http://orcid.org/0000-0001-6944-9883
Alaaddin Cukurovali http://orcid.org/0000-0002-8297-2350
İbrahim Kani http://orcid.org/0000-0002-7654-6013

References

[1] R.S. Moraes, R.E. Aderne, M. Cremona, and N.A. Rey, Opt. Mater. (Amst) **52**, 186–191 (2016).

[2] X. Cao, X. Zeng, L. Mu, Y. Chen, R.-x. Wang, Y.-q. Zhang, J.-x. Zhang, and G. Wei, Sens. Actuator. B **177**, 493–499 (2013).

[3] M.-J. Park, J.-H. Lee and D.-H. Hwang, Curr. Appl. Phys. **6** (4), 752–755 (2006).

[4] R. Laurinaviciute, V. Mimaite, J. Ostrauskaite, J.V. Grazulevicius, and V. Jankauskas, Synth. Met **197**, 1–7 (2014).

[5] D. Singhal, N. Gupta, and A.K. Singh, Mater. Sci. Eng. C **58**, 548–557 (2016).

[6] V.K. Gupta, A.K. Singh, S. Bhardwaj, and K.R. Bandi, Sens. Actuator. B **197**, 264–273 (2014).

[7] M. Bakir and C. Gyles, J. Mol. Struct. **753** (1–3), 35–39 (2005).

[8] Z. Yan, H. Wang, C. Xu, X. Wen, and B. Gu, J. Mol. Liq. **190**, 185–189 (2014).

[9] S. Swami, A. Agarwala, B. Malik and R. Shrivastava, J. Chem. Sci. **128** (9), 1451–1457 (2016).

[10] Y.-R. Chiou, C.-F. Wan and A.-T. Wu, J. Fluoresc. **27** (1), 317–322 (2017).

[11] C. deMilt and G.v. Zandt, J. Am. Chem. Soc. **58** (10), 2044–2046 (1936).

[12] G. Hallas and A.D. Towns, Dyes. Pigm. **33** (4), 319–336 (1997).

[13] A. Towns, Dyes. Pigm. **42** (1), 3–28 (1999).

[14] M.J. O'Neil, A. Smith, P. Heckelman, Inc., Whitehouse Station, NJ 6596 (2001).

[15] G. Ayhan-Kılcıgil, C. Kus, E.D. Özdamar, B. Can-Eke and M. Iscan, Arch. Pharm. (Weinheim). **340** (11), 607–611 (2007).

[16] C. Kus, G. Ayhan-Kilcigil and B.C. Eke, Arch. Pharm. Res. **27** (2), 156 (2004).

[17] L. Li, Z. Li, K. Wang, Y. Liu, Y. Li and Q. Wang, Bioorg. Med. Chem. **24** (3), 474–483 (2016).

[18] S. Issaadi, T. Douadi, A. Zouaoui, S. Chafaa, M. Khan and G. Bouet, Corros. Sci. **53** (4), 1484–1488 (2011).

[19] K.H. Reddy, P.S. Reddy and P.R. Babu, Transit. Met. Chem. **25** (5), 505–510 (2000).

[20] D. Hadjipavlou-Litina and A. Geronikaki, Arzneimittelforschung. **46** (8), 805–808 (1996).

[21] B.S. Holla, K. Malini, B.S. Rao, B. Sarojini and N.S. Kumari, Eur. J. Med. Chem. **38** (3), 313–318 (2003).

[22] A. Bruker, Bruker AXS Inc., Madison, Wisconsin, USA (2008).

[23] O.V. Dolomanov, L.J. Bourhis, R.J. Gildea, J.A. Howard and H. Puschmann, J. Appl. Crystallogr. **42** (2), 339–341 (2009).

[24] G.M. Sheldrick, Acta Crystallogr. A. **71** (1), 3–8 (2015).

[25] G.M. Sheldrick, Acta Crystallogr. C. **71** (1), 3–8 (2015).

[26] M. Frisch, G. Trucks, H.B. Schlegel, G. Scuseria, M. Robb, J. Cheeseman, G. Scalmani, V. Barone, B. Mennucci, G. Petersson, Inc., Wallingford, CT 200 (2009).

[27] A.D. Becke, J. Chem. Phys. **98** (7), 5648–5652 (1993).

[28] C. Lee, W. Yang and R.G. Parr, Phys. Rev. B. **37** (2), 785 (1988).

[29] J.B. Foresman and A. Frisch, *Exploring Chemistry with Electronic Structure Methods*, 2nd ed. (Gaussian Inc., Pittsburg, 1996).

[30] R. Dennington, T. Keith, J. Millam, K. Eppinnett, W.L. Hovell, R. Gilliland, GaussView, Version (2009).

[31] P. Giannozzi, S. Baroni, N. Bonini, M. Calandra, R. Car, C. Cavazzoni, D. Ceresoli, G.L. Chiarotti, M. Cococcioni and I. Dabo, J. Phys. Condens. Mat. **21** (39), 395502 (2009).

[32] P. Hohenberg and W. Kohn, Phys. Rev. **136** (3B), B864 (1964).

[33] J.P. Perdew and A. Zunger, Phys. Rev. B. **23** (10), 5048 (1981).

[34] J.P. Perdew, K. Burke and M. Ernzerhof, Phys. Rev. Lett. **77** (18), 3865 (1996).

[35] M.A. Spackman and D. Jayatilaka, Cryst. Eng. Comm. **11** (1), 19–32 (2009).

[36] M. Turner, J. McKinnon, S. Wolff, D. Grimwood, P. Spackman, D. Jayatilaka, M. Spackman, CrystalExplorer17, University of Western Australia Crawley, Western Australia, Australia (2017).

[37] T.A. Keith, There is no corresponding record for this reference (2016).

[38] T. Karakurt, Acta Crystallogr. C **74** (11), 1502–1508 (2018).

[39] A. Cukurovali and T. Karakurt, J. Mol. Struct. **1189**, 328–337 (2019).

[40] M.J. Dewar, E.G. Zoebisch, E.F. Healy and J.J. Stewart, J. Am. Chem. Soc. **107** (13), 3902–3909 (1985).

[41] H.J. Monkhorst and J.D. Pack, Phys. Rev. B. **13** (12), 5188 (1976).

[42] J.P. Merrick, D. Moran and L. Radom, J. Phys. Chem. A. **111** (45), 11683–11700 (2007).

[43] R. Silverstein, G. Bassler, and T. Morrill, Spectromet. Ident. Organ. Comp **30**, 364 (1981). New York, John Wiley and Sons.

[44] H.A. Dabbagh, A. Teimouri, A.N. Chermahini and M. Shahraki, Spectrochim. Acta Part A. **69** (2), 449–459 (2008).

[45] D.M. Smith, Benzimidazoles and Cogeneric Tricyclic Comp **130**, 331 (2009).

[46] T. Karakurt, A. Cukurovali, N.T. Subasi, A. Onaran, A. Ece, S. Eker, and I. Kani, Chem. Phys. Lett **693**, 132–145 (2018).

[47] G. Varsányi, *Assignments for Vibrational Spectra of Seven Hundred Benzene Derivatives* (Halsted Press, New York, 1974).

[48] R. Ditchfield, J. Chem. Phys. **56** (11), 5688–5691 (1972).

[49] P. Pulay, K. Wolinski, and J. Hinton, J. Am. Chem. Soc **112**, 8251–8260 (1990).

[50] D. Mahadevan, S. Periandy, M. Karabacak, S. Ramalingam, and N. Puviarasan, Spectrochim. Acta Part A **86**, 139–151 (2012).

[51] S. Murugavel, V.V. Velan, D. Kannan, and M. Bakthadoss, J. Mol. Struct **1108**, 150–167 (2016).

[52] C. Selvaraj and S.K. Singh, J. Biomol. Struct. Dyn. **32** (8), 1333–1349 (2014).

[53] M. Er, B. Ergüven, H. Tahtaci, A. Onaran, T. Karakurt and A. Ece, Med. Chem. Res. **26** (3), 615–630 (2017).

[54] S. Jenkins and I. Morrison, Chem. Phys. Lett. **317** (1–2), 97–102 (2000).

[55] R.F. Bader and H. Essén, J. Chem. Phys. **80** (5), 1943–1960 (1984).

[56] I. Rozas, I. Alkorta and J. Elguero, J. Am. Chem. Soc. **122** (45), 11154–11161 (2000).

[57] A. Shukla, E. Khan, P. Tandon, and K. Sinha, J. Mol. Struct. **1131**, 225–235 (2017).

[58] M. Rocha, D.M. Gil, G.A. Echeverrí, O.E. Piro, J.L. Jios and S.E. Ulic, J. Org. Chem. **84**, 11042–11053 (2019).

[59] E. Espinosa, E. Molins and C. Lecomte. Chem. Phys. Lett. **285** (3), 170–173 (1998).

[60] S.A. Nami, N. Sarikavakli, M.J. Alam, M. Alam, S. Park, and S. Ahmad, J. Mol. Struct **1138**, 90–101 (2017).

[61] P. Venkatesan, S. Thamotharan, A. Ilangovan, H. Liang, and T. Sundius, Spectrochim. Acta Part A **153**, 625–636 (2016).

[62] J.B. Collins, P.v.R. Schleyer, J.S. Binkley and J.A. Pople, J. Chem. Phys. **64** (12), 5142–5151 (1976).

[63] W.J. Hehre, R.F. Stewart and J.A. Pople, J. Chem. Phys. **51** (6), 2657–2664 (1969).

[64] A. Saeed, S. Ashraf, U. Flörke, Z.Y.D. Espinoza, M.F. Erben, and H. Pérez, J. Mol. Struct. **1111**, 76–83 (2016).

[65] E. Torabi Farkhani, M. Pourayoubi, M. Izadyar, P.V. Andreev, and E.S. Shchegravina, Acta Crystallogr. C **74** (7), 847–855 (2018).

[66] C.F. Mackenzie, P.R. Spackman, D. Jayatilaka and M.A. Spackman, IUCrJ. **4** (5), 575–587 (2017).